Dissociation of hydrogen and formation of water at the (010) and (111) surfaces of orthorhombic $FeNbO_4$

Xingyu Wang[1], David Santos-Carballal[1], Nora H. de Leeuw[1,2*]

[1] School of Chemistry, University of Leeds, Leeds LS2 9JT, United Kingdom

[2] Department of Earth Sciences, Utrecht University, 3584 CB Utrecht, The Netherlands

n.h.deleeuw@leeds.ac.uk

Abstract

The orthorhombic structure of $FeNbO_4$, where the Fe and Nb cations are distributed randomly over the octahedral 4c sites, has shown excellent promise as an anode material in solid oxide fuel cells. In this study, we have used calculations based on the density functional theory with a Hubbard Hamiltonian and long-range dispersion corrections (DFT+U-D2) to explore the adsorption and dissociation of H_2 molecules and the formation reaction of water at the (010) and (111) surfaces. We have generated pristine surfaces with random distributions of cations from a 2×2×2 quasi-random orthorhombic bulk structure. Specifically, we have considered various terminations for the (010) and (111) surfaces with different ratios of Fe and Nb cations in the exposed layers. The top and sub-surface layers of the (010) surface move in opposite directions after relaxation, whereas the relaxed layers of the (111) surface shift outward by no more than 2.5%. Simulations of the surface properties confirmed that the bandgaps are significantly reduced compared to the bulk material. We found that the hydrogen molecule prefers to dissociate at the O bridge sites of the (010) and (111) surfaces, especially where these are coordinated to Fe cations, thereby forming two hydroxyl groups. We have investigated the water formation reaction and found that the energy

barriers for migration of the H ions are generally lower for the Fe/Nb-O sites than for the O-O site. Overall, our simulations predict that after dissociation, the H atoms tend to remain stable in the form of O_{layer}-H groups, whereas a larger barrier needs to be overcome to achieve the formation of water. Future work will focus on potential surface modifications to reduce further the barrier of migration of the dissociated H ions, especially from the oxygen bridge sites.

1. Introduction

Climate change and air pollution have become a global crisis that affects the whole of society. One way to reduce the risk of escalation is to deploy alternative green energy sources, like hydrogen, to replace traditional fossil fuel sources. Hydrogen is considered as one of the most promising sources to achieve a sustainable energy future, due to its abundant reserves in the form of water and its renewability[1-12].

Solid oxide fuel cells (SOFCs), which consist of solid-state cathode, electrolyte and anode, are devices of particular interest, since they have high efficacy and the ability to process different fuels, including hydrogen, hydrocarbons and carbon monoxide, under medium and high temperatures (above 700 °C) to produce electricity[1-4]. At the anode, reactions take place where fuel gases are oxidized to CO_2 or H_2O, providing electrons to the external circuit. Over the past years, Ni metal has been considered a good anode material, owing to its low cost, good catalytic ability and high electronic conductivity[5-7]. However, Ni-metal anodes have shown poor tolerance to sulfur and carbon deposition[1, 3-4, 6], which limits the chemical activity under long-term operation. As a result, several alternative ceramic materials, such as CeO_2 and $La_{0.75}Sr_{0.25}CrO_3$ (LSCr),[6, 8-12] have been developed to replace Ni metal as the anode material in SOFCs. Those oxide anode materials offer resistance to carbon deposition and stability during the operation of SOFCs at high temperatures, but they show lower catalytic efficiency and electronic conductivity than Ni-metal anodes[6].

In addition to the CeO_2 and LSCr anode materials, research on Fe-based materials, *i.e.*

$LaFeO_3$, $FeVO_4$, and $FeNbO_4$, has also made significant progress[13-19]. For example, previous studies have shown that orthorhombic $FeNbO_4$ materials are good catalysts for hydrogen dissociation above 700 °C, where Nb^{5+} cations remain stable while Fe^{3+} cations are reduced to Fe^{2+} under an H_2 atmosphere. In contrast to many other Fe-based oxides, the Fe and Nb cations are distributed randomly in the orthorhombic structure (o-$FeNbO_4$) and thus layers consisting of only Fe^{3+} cations do not exist, see Figure 1. Furthermore, the random distribution of Fe^{3+}-Fe^{2+} chains throughout the whole material under operation ensures that electrons can be conducted along the 3D Fe-O-Fe network and continuous reduction of Fe^{3+} in the same layer can be avoided, which explains why the o-$FeNbO_4$ phase has good structural stability and relatively high electronic conductivity[14, 16].

The reaction mechanisms for the oxidation of fuels, especially hydrogen, at the surfaces of o-$FeNbO_4$ is not as yet well understood. In this work, we have selected the (010) and (111) surfaces of o-$FeNbO_4$, which in previous have been shown to be the dominant surfaces,[20] to explore their activity towards the H_2 molecule. Random distributions of cations and different stacking sequences of the surfaces have been considered to simulate realistic disordered o-$FeNbO_4$ configurations. We have used calculations based on the density functional theory with a Hubbard Hamiltonian and long-range dispersion corrections (DFT+U-D2) to study the surface properties and reactions with the H_2 molecule, including the dissociation of H_2, diffusion of H atoms and formation of water at the surface.

2. Computational methods

The Vienna Ab initio Simulation Package, VASP (version 5.4.4), has been employed to carry out the DFT calculations.[22-25] In all calculations, the ion-electron interactions were described by the projector-augmented wave method (PAW)[26]. The following electrons were treated as valence electrons: Fe ($3p^6 3d^7 4s^1$), Nb ($4p^6 5s^1 4d^4 4s^2$), O ($2s^2 2p^4$) and H ($1s^1$). We have employed the Perdew-Burke-Ernzerhof (PBE) generalized gradient

approximation (GGA) functional to perform all spin-polarized simulations[27]. To enhance the accuracy of the description of the electronic structures, the on-site Coulombic interaction (DFT+U) introduced by Dudarev et al[28] was chosen for the Fe 3d electrons with a U_{eff} value of 4.3 eV[29-30]. The kinetic energy cutoff for the plane waves was set at 500 eV and all calculations were performed using the tetrahedron method with Blöchl corrections. The Henkelman algorithm was used to calculate Bader charges[31]. A 2×2×2 supercell with random distributions of cations and a spin-glass phase, comprising 16 Fe, 16 Nb and 64 O (Figure 1), was obtained via the special quasi-random structures (SQS) method, which is based on a Monte Carlo simulated annealing loop with an objective function designed to perfectly match the maximum number of correlations[32]. This method is implemented in the Alloy Theoretic Automated Toolkit (ATAT)[33-35]. Specifically, Fe_5Nb_3, Fe_3Nb_5, Fe_3Nb_5 and Fe_5Nb_3 were distributed alternately along a direction in the 2×2×2 supercell. We have used the METADISE code[36] to create the reconstructed dipolar (010) and (111) surfaces from the 2×2×2 supercell. The surface models consist of slabs of 8 layers along [010] and 4-layer repeat units along [111], respectively, with 12 Å vacuum space in between the slabs and their images in neighbouring cells. 3×3×3, 2×2×1 and 3×3×3 gamma-centered Monkhorst Pack grids were used for the simulations of the bulk, surface slabs, and isolated hydrogen/water molecules in a 10 Å × 10 Å × 10 Å cubic box, respectively. All calculations of the surface and bulk were carried out with the DFT-D2 method implemented in VASP to incorporate the Van der Waals correction[37]. The D2 parameters used were the pre-determined C_6 values of 10.80 $J \cdot nm^6 \cdot mol^{-1}$, 19.40 $J \cdot nm^6 \cdot mol^{-1}$, 5.71 $J \cdot nm^6 \cdot mol^{-1}$ and 0.14 $J \cdot nm^6 \cdot mol^{-1}$, and the R_0 values of 1.485 Å, 1.908 Å, 1.342 Å and 1.001 Å were used for the Fe, Nb, O and H atoms, respectively. All geometry optimizations in this work were performed with the conjugate gradient method with a convergence criterion of 0.01 eV/Å. The scanning tunnelling microscopy (STM) images of the exposed surfaces were calculated using the Tersoff-Hamman approach, where the STM tip approximates an infinitely small point source, as implemented in HIVE[38].

In terms of the optimization of the surfaces, we fixed the bottom 50% of atomic layers at their relaxed bulk positions, whereas the top 50% were allowed to relax unconstrainedly to obtain the optimized surfaces. The Bader charges and magnetic moments of the surface atoms are calculated using an improved grid-based algorithm and the work function is obtained using the following equation:

$$\Phi = E_{vac} - E_F \quad (1)$$

where E_{vac} is the vacuum level and E_F is the Fermi level of the surfaces.

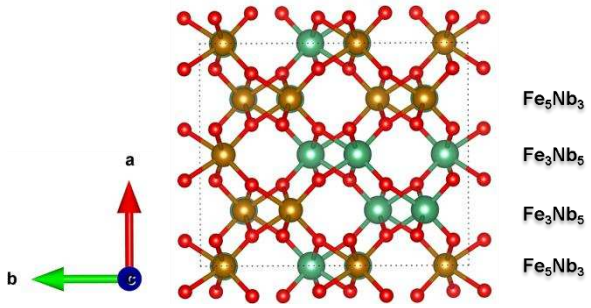

Figure 1. 2×2×2 supercell of the orthorhombic $FeNbO_4$ structure obtained from the ATAT model; O atoms are red; Fe atoms are yellow; Nb atoms are green.

The Helmholtz free energy of the dissociation process of H_2 was calculated using:

$$\Delta F = \Delta E + \Delta E_{ZPE} - T\Delta S \quad (2)$$

where ΔE, ΔE_{ZPE}, and ΔS are the variation of the electronic energy obtained from the DFT calculations, the zero-point energy correction, and the vibrational contribution to the entropy, respectively. We have calculated the vibrational frequencies by relaxing only the adsorbed atoms (H and H_2O molecules), and then obtained the ΔE_{ZPE} and ΔS values via the VASPKIT code[39]. VASPKIT employs the harmonic approximation to calculate the entropy contribution to the free energy as:

$$\boldsymbol{E_{ZPE} = \frac{1}{2}\sum_i \hbar\omega_i}$$

$$\mathrm{TS} = \mathrm{RT}\{\sum_i \frac{\frac{\hbar\omega_i}{k_B T}}{\exp\left(\frac{\hbar\omega_i}{k_B T}\right) - 1} - \sum_i \ln\left[1 - \exp\left(-\frac{\hbar\omega_i}{k_B T}\right)\right]\}$$

where $\boldsymbol{\omega_i}$ are the vibrational frequencies, R and k_B are the gas constant and

Boltzmann constant, respectively. The experimental entropy ΔS for gaseous H_2 was obtained from the NIST database[41].

The energy for the dissociation of H_2 can be expressed as:

$$\Delta E = E_{sur+H_2} - E_{sur} - E_{H_2} \quad (3)$$

where E_{sur+H_2} represents the total energy of the surface with adsorbed dissociated hydrogen, E_{sur} represents the total energy of the pristine surface and E_{H_2} represents the energy of the isolated H_2 molecule.

We employed the climbing image nudged elastic band (CI-NEB) method to study the transition states of the surface migration of the H ions. To find the transition states, we inserted five consecutive images along the minimum energy path (MEP) from the dissociation of hydrogen to the formation of water to calculate saddle points, where the calculations were carried out using the limited memory Broyden Fletcher Goldfarb Shanno (LBFGS) method[40] until the forces were smaller than 0.05 eV/Å. We confirmed that each transition state had an imaginary vibrational frequency along the reaction direction.

3. Results and Discussion

Previous work[42-44] has shown, that the (010) and (111) surfaces are the two dominant surfaces of $FeNbO_4$. In this work, we have therefore focused on these two surfaces and created simulation cells of 8 layers for the different (010) terminations and 4 repeat units for the (111) surface, see Figures 2 and 3. The stacking sequences in the (010) surfaces are -Fe_3NbO_8-$Fe_2Nb_2O_8$-$FeNb_3O_8$-, which are reconstructed Tasker type III surfaces. The Tasker type I (111) surface shows a stacking sequence of -$Fe_8Nb_8O_{32}$-$Fe_8Nb_8O_{32}$- along the z axis. In addition, we found that the exposed cations in the topmost layers of the (010) surfaces are coordinated by four oxygen atoms, forming two dangling bonds towards the vacuum. Thus, we have three terminations for the (010) surface, *i.e.* the $(FeO_4)_3(NbO_4)_1$, the $(FeO_4)_2(NbO_4)_2$ and the $(FeO_4)_1(NbO_4)_3$ terminations, which are henceforth called Fe_3Nb_1, Fe_2Nb_2 and Fe_1Nb_3 terminations, respectively, in the following discussion.

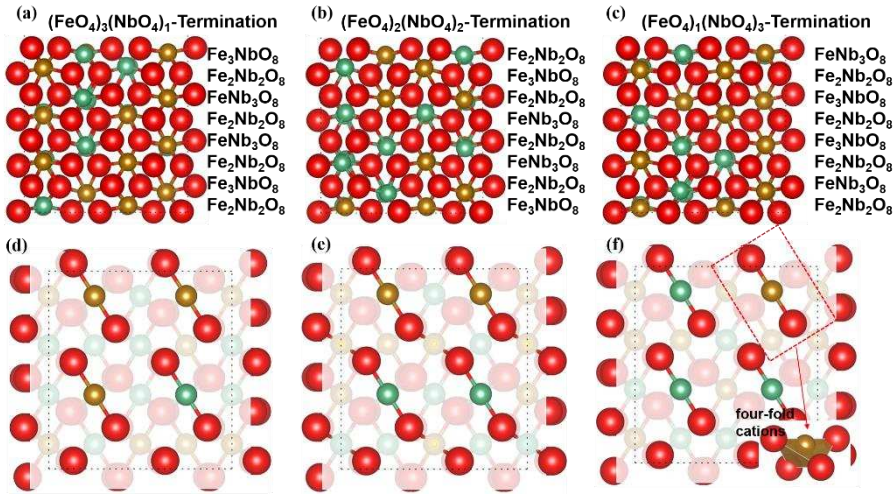

Figure 2. Side view (a-c) and top view (d-e) of the three (010) surfaces and their corresponding stacking sequences; O atoms are red; Fe atoms are yellow; Nb atoms are green.

In contrast, each layer in the (111) surface comprises the same number of cations and we have therefore only explored the surface properties of one termination and its interactions with the H_2 molecule. It is worth noting that in the top layers the two Fe and two Nb cations are fully coordinated by oxygen, whereas the other six Fe and six Nb are five-fold coordinated cations, leading to one dangling bond each towards the vacuum, see Figure 3. From here on, we will denote the $(FeO_5)_6(FeO_6)_2(NbO_5)_6(NbO_6)_2$-termination as Fe_8Nb_8.

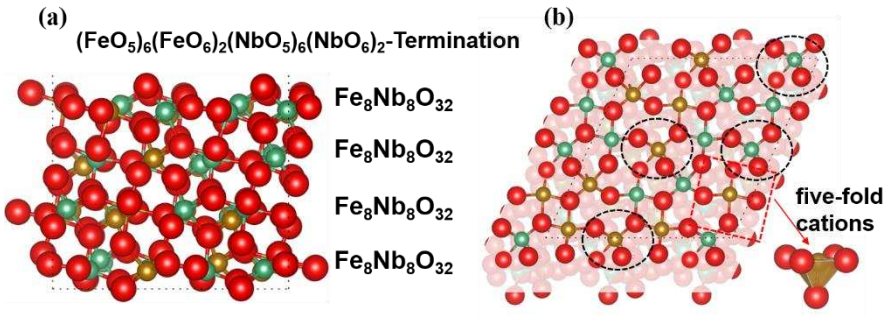

Figure 3. Side view (a) and top view (b) of the (111) surfaces and their corresponding stacking sequences; the black ellipse refers to the Fe/NbO_6; O atoms are red; Fe atoms are yellow; Nb atoms are green.

3.1 Surface properties

First, we have calculated the Bader charges, magnetic moments and work functions of the four surfaces, listed in Table 1, where the Bader charges and magnetic moments of the surface models are the average values of the exposed ions. Our simulations show that the Bader charge of the fully coordinated Fe cations in the bulk model is larger than that of the Fe cations with dangling bonds in the surfaces. Similar trends can be found for the Bader charges of the Nb and O ions, i.e. the Bader charges of the exposed ions are slightly smaller than those in the bulk structure. The magnetic moment of the Fe cations in the bulk is 4.21 μ_B, which is reduced to 4.18, 4.16, 4.15 and 4.19 μ_B for the Fe_3Nb_1, Fe_2Nb_2, Fe_1Nb_3 and Fe_8Nb_8 surfaces, respectively. We found that the Nb and O ions in both the bulk and surface models have zero magnetic moments. The calculated work function of the Fe_1Nb_3-terminated (010) surface is 7.29 eV, which is significantly larger than the other three surfaces.

In general, our simulations indicate that the Bader charges and the magnetic moments of the exposed ions are partially dependent on the coordination numbers. For instance, the five-coordinated Fe and Nb cations in the (010) surfaces have larger values of q and m_s than the four-coordinated cations in the (111) surface, indicating that the five-fold cations are in a higher oxidation state than their four-fold counterparts. In addition, we found that the work functions of the (010) surfaces are generally smaller than that of the (111) surface, with the exception of the Fe_1Nb_3-terminated (010) surface, suggesting that the number of exposed Nb cations can negatively affect the surface reactivity.

Table 1. Average Bader charge (q) and the average magnetic moment (m_s) of the ions on the top layers and the work function.

	q_{Fe}(e)	q_{Nb}(e)	q_O(e)	m_{sFe}(μB)	m_{sNb}(μB)	m_{sO}(μB)	Φ(eV)
Bulk	+1.84	+2.71	-1.14	4.21	0	0	-
Fe_3Nb_1-Termination	+1.76	+2.62	-1.06	4.18	0	0	5.44
Fe_2Nb_2-Termination	+1.75	+2.62	-1.06	4.16	0	0	5.13
Fe_1Nb_3-Termination	+1.73	+2.59	-1.04	4.15	0	0	7.29
Fe_8Nb_8-Termination	+1.79	+2.63	-1.03	4.19	0	0	6.02

Figure 4 shows the interplanar relaxations of the three (010) and the (111) surfaces, which were defined as the difference between the atomic layers in the surface relative to their positions in the bulk structure. It can be calculated through $\Delta_{ij} = 100(d_{ij} - d_{ij}^{\circ})/d_{ij}^{\circ}$, where d_{ij} and d_{ij}° represent the separation between the relaxed *i*-th and $j = i+1$-th atomic layers in the surface model and in the bulk model, respectively. As mentioned above, the Fe_3Nb_1, Fe_2Nb_2 and Fe_1Nb_3 terminations contain eight layers, namely FeNbO-1 to FeNbO-8, whereas four layers constitute the (111) surface model and we have plotted the data from FeNbO-1 to FeNbO-4. Our simulations suggest that after relaxation the topmost layer FeNbO-1 of the three (010) surfaces moves towards the bulk by 6.7 %, 8.71 % and 0.55 % in the Fe_3Nb_1, Fe_2Nb_2 and Fe_1Nb_3 surfaces, respectively. The subsequent layers from FeNbO-2 to FeNbO-4 experienced gradually decreased relaxation outwards from the bulk from 6.4 to 1.7% and 5 to 0.5% for the Fe_3Nb_1 and Fe_2Nb_2 terminations, respectively, whereas the Fe_1Nb_3 termination suffered the maximum relaxation of 3.6% outwards from the bulk in the FeNbO-3 layer. For the Fe_8Nb_8 surface we found that the topmost FeNbO-1 layer shifts outwards by 2.5% which trend decreased to 0.55% for the sub-FeNbO-2 layer.

Overall, our calculations indicate that the relaxations of the FeNbO-1 and FeNbO-2 layers oppose each other and thus, those two layers tend to merge to form the exposed surface. In contrast, we found that both the two relaxed layers of the (111) surface move outward from the bulk by no more than 2.5%.

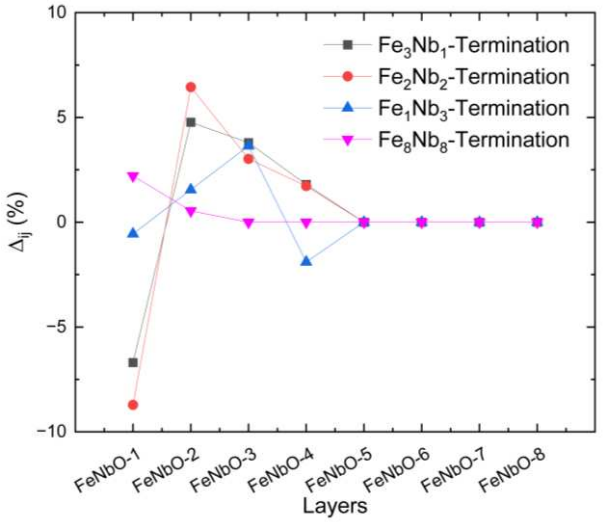

Figure 4. Interplanar distances of the four surfaces.

Next, we generated STM images at a bias of -3.5 eV, which are plotted in Figure 5. We found that the brightest spots represent the oxygen atoms, whereas the cations cannot be identified very well owing to their low resolution. The presence of cations from the sub-surface layers can be seen on the (010) surfaces, in agreement with the analysis of the interplanar relaxation. In addition, our simulations suggest that the array of O-Fe/Nb-O-Fe/Nb appears along the $[\bar{1}0\bar{1}]$ direction in the (010) surfaces, and similarly the five-fold Fe/Nb cations are distributed along the $[\bar{1}10]$ direction in the (111) surface.

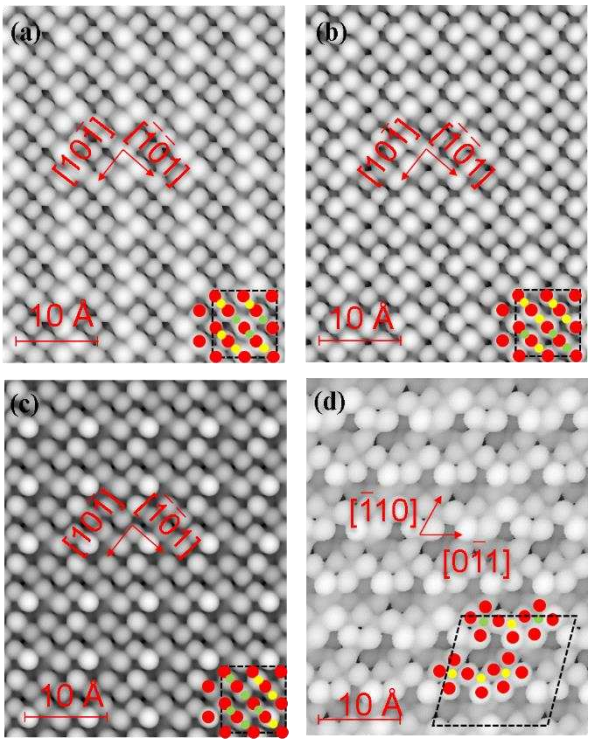

Figure 5. Scanning tunneling microscopy (STM) images of (a-c) the Fe_3Nb_1-, Fe_2Nb_2- and Fe_1Nb_3 terminations of the 010 surface, respectively; (d) the Fe_8Nb_8-termination of the (111) surface; O atoms are in red; Fe atoms are in yellow; Nb atoms are in green.

Finally, we have simulated the partial densities of states (PDOS) of the four surfaces, see Figure 6. The localized t_{2g} and e_g orbitals of the Fe ions near -8 eV are distributed over both the major and minor spin channels on the four surfaces, whereas the 3d states of Nb and 2p states of O are delocalized in the wide valence region from -8 to 0 eV. The unoccupied conduction region is mainly composed by the d states of the metal cations at those surfaces. In addition, our simulations indicate that in the (010) surfaces, the band gap decreases with the numbers of exposed four-fold Fe cations, suggesting the sequence: $E_{bandgap}^{Fe3Nb1} < E_{bandgap}^{Fe2Nb2} < E_{bandgap}^{Fe1Nb3}$. In general, we found that the band gaps in the surfaces are significantly reduced compared to the bulk material,[20] because the existing metal-oxygen dangling bonds in the exposed surface layers can behave as chemically active sites, as was also found in other studies[44-49].

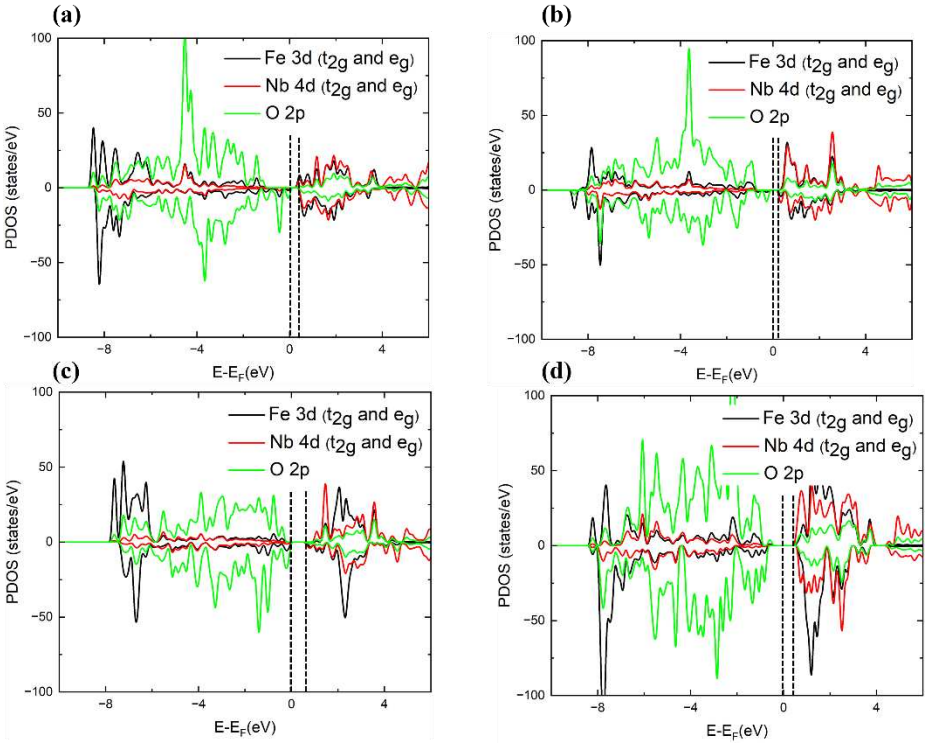

Figure 6. Projected density of states (PDOS) of the $FeNbO_4$ surfaces: (a-c) Fe_3Nb_1-, Fe_2Nb_2- and Fe_1Nb_3 terminations of the 010 surface, respectively; (d) Fe_8Nb_8-termination of the (111) surface

3.2 Dissociation of H_2

In our previous study[20], we found that the (010), (110), and (011) surfaces have similar exposed reaction sites. In this work, we have therefore focused on the (010) and (111) surfaces, including a number of distinct surface sites owing to the cation disorder in the orthorhombic $FeNbO_4$ phase, to explore the catalytic reactions of hydrogen molecules at the surface. In a real disordered orthorhombic $FeNbO_4$ structure, it is believed that the dissociation reactions of hydrogen take place at the surfaces, where Fe and Nb cations are distributed randomly. In this work, the four generated surfaces display random distributions of cations on a 2×2 scale. To explore the mechanisms of the surface reactions, we have only introduced one hydrogen molecule and placed it at different sites to investigate how the surface ions affect the dissociation reactions. We have classified two types of reaction sites for the dissociation of H_2 and the formation of H_2O on the (010) and (111) surfaces. One is defined as an Fe/Nb-O site which

involves one cation site and its nearest oxygen site. The other one is an oxygen-oxygen site comprising two adjacent oxygen atoms, each coordinated by two cations, and is therefore labeled as $O_{A1B1\text{-}A2B2}$, where the subscript A1B1 and A2B2 represents the cations to which the oxygens are bonded.

3.2.1 (010) surface

As shown in Figure 7, the Fe/Nb cations are coordinated by four oxygen ions in the exposed layers of the (010) surfaces. We identified three types of surface moieties, *i.e.* Fe-O-Fe, Fe-O-Nb and Nb-O-Nb on the (010) surfaces, creating two metal-oxygen and six oxygen-oxygen dissociation sites, which are represented by Fe-O, Nb-O $O_{FeFe-FeFe}$, $O_{FeFe-FeNb}$, $O_{FeFe-NbNb}$, $O_{FeNb-FeNb}$, $O_{NbNb-FeNb}$ and $O_{NbNb-NbNb}$, respectively, see Figure 7. It is worth noting that we did not consider the $O_{NbNb-NbNb}$, $O_{NbNb-NbNb}$, and $O_{FeFe-FeFe}$ sites on the Fe_3Nb_1 Fe_2Nb_2 and Fe_1Nb_3 terminations, respectively, owing to the lack of Nb and Fe cations in the top and sub-surface layers.

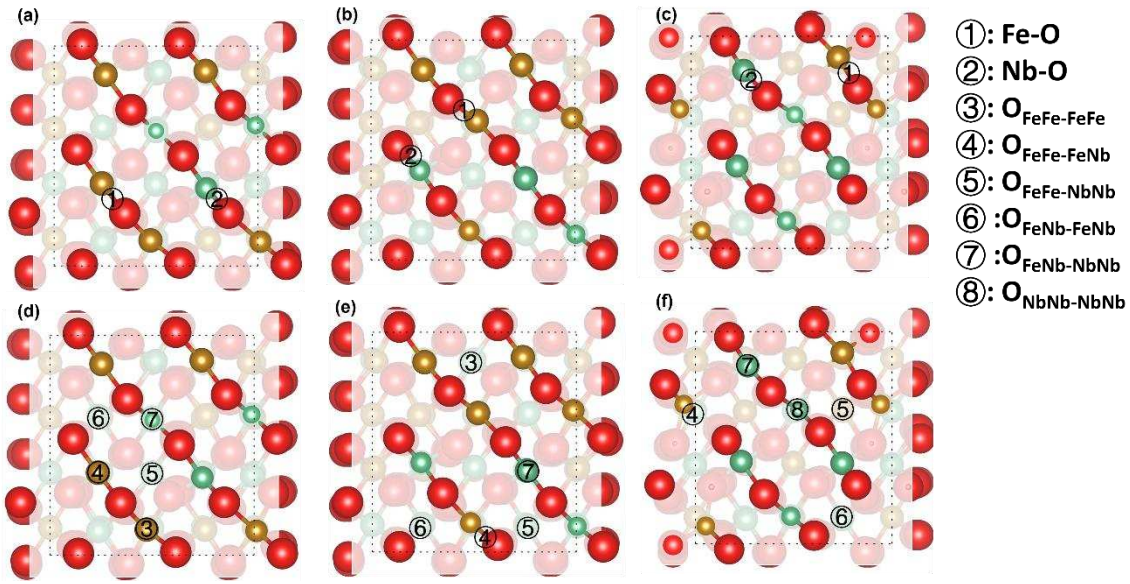

Figure 7. Top view of the Fe/Nb-O dissociation sites (a-c) and O-O sites (d-f) of the (010) surfaces; (a,d) Fe_3Nb_1-termination; (b,e) Fe_2Nb_2-termination; (c,f) Fe_1Nb_3-termination; O atoms are red; Fe atoms are yellow; Nb atoms are green, shading is used to enhance the visibility of the top atomic layers.

First, we have calculated the dissociation energies at all sites on the surfaces from 0 to 900 K, see Figure 8. Our simulations show that the dissociation of H_2 at the $O_{FeFe-FeFe}$ and $O_{FeFe-FeNb}$ sites of Fe_3Nb_1 and Fe_2Nb_2 terminations remains energetically favorable from 0 to 900 K, whereas the reactions at other sites, *i.e.* the $Fe-O$, $Nb-O$, $O_{FeFe-NbNb}$, $O_{FeNb-FeNb}$ and $O_{NbNb-FeNb}$ sites, become endothermic processes as the temperature rises. In particular, we found that dissociation at the $O_{NbNb-FeNb}$ sites is significantly endothermic even at 0 K. On the Fe_1Nb_3 termination the $O_{FeFe-FeNb}$ and $O_{FeFe-NbNb}$are the two thermodynamically favorable sites between 0 to 900 K, with the dissociation energy ranging from -1.96 to -1.57 eV and -1.54 to -0.18 eV, respectively, whereas the reactions at the $O_{FeNb-FeNb}$, $O_{NbNb-FeNb}$, $O_{NbNb-NbNb}$, $Fe-O$ and $Nb-O$ sites become endothermic from 900 K, 600 K, 600 K, 300 K and 0 K, respectively.

Overall, our simulations indicate that the dissociation energies on all the surfaces increase with temperature and the energies on the Fe_3Nb_1 and Fe_2Nb_2 terminations show the same order of $E_{NbNb-NbFe} < E_{Nb-O} < E_{Fe-O}, < E_{FeFe-NbNb} < E_{FeNb-FeNb} < E_{FeFe-FeNb} < E_{FeFe-FeFe}$, whereas the order changes into $E_{Nb-O} < E_{Fe-O} < E_{NbNb-NbNb} < E_{FeNb-FeNb} < E_{NbNb-FeNb} < E_{FeFe-NbNb} < E_{FeFe-FeNb}$ on the Fe_1Nb_3 termination. Interestingly, on the one hand we found that the number of Fe cations coordinated to the O sites can affect the dissociation energy. For instance, the H_2 molecule prefers to be dissociated at the $O_{FeFe-FeFe}$ and $O_{FeFe-FeNb}$ sites, with respect to the $O_{NbNb-NbNb}$ and $O_{NbNb-NbFe}$ sites. On the other hand, the dissociation energies at the $O_{FeFe-FeFe}$ and $O_{FeFe-FeNb}$ sites of the three (010) surfaces are in agreement with the trend in the work functions, shown in Table 1.

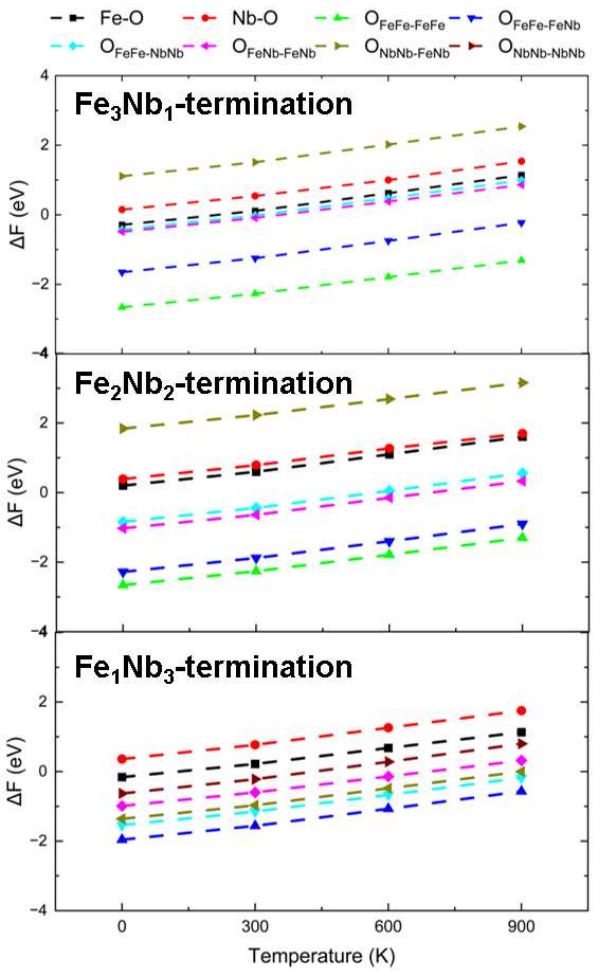

Figure 8. Dissociation energy of H_2 on the (010) surfaces from 0 to 900 K.

In previous work[44-48], the dissociation of the hydrogen molecule at the O sites has been studied extensively and H atoms coordinated by oxygen are generally oxidized after dissociation. To explore how the electrons are transferred at the metal-oxygen sites in this work, we have focused on the charge transfer and other properties, *i.e.* Bader charge and bond length, at the Fe/Nb-O sites, see Figure 9.

Our simulations suggest that the H atoms from the O-H and the Fe/Nb-H groups are surrounded by electron depletion and gain areas, respectively. Correspondingly, a relatively small gain and depletion area is distributed around the O and Fe/Nb atoms, respectively. We found that the electron depletion area around the hydroxyl at the Nb-O site is slightly larger than that at the Fe-O site. The calculated Bader charge of the H for the hydroxyl ranges from +0.60 to +0.67, whereas the H atoms coordinated by Fe have Bader charges of -0.19 to -0.29, which is smaller than those bound to Nb, see Table

2. In addition, we have shown the bond lengths in Figure 9, where the Fe-H bond at 1.79 Å is slightly longer than the Nb-O bond (1.76 Å) on the Fe_3Nb_1 terminations. In contrast, in the Fe_2Nb_2 and Fe_1Nb_3 terminations, the Nb-O bond length is longer than that of Fe-O, because on the Fe_3Nb_1 termination the Fe cation in the sub-surface layer exhibits similar chemical activity towards the dissociated H atom, which therefore tends to move closer to this Fe atom at a distance of 1.91 Å after optimization. An O-H bond length of approximately 0.98 Å was measured in all the hydroxyl groups. Overall, our simulations demonstrate that after dissociation at the metal-oxygen sites, one H atom becomes bonded tightly to the oxygen, forming a hydroxyl group, whereas another H atom is captured by the surrounding metal cations, forming the relatively weak Fe/Nb-H bond. In this process, electrons are transferred from one dissociated H atom to the coordinated O atom, whereas the other H atom obtains electron from the metal site.

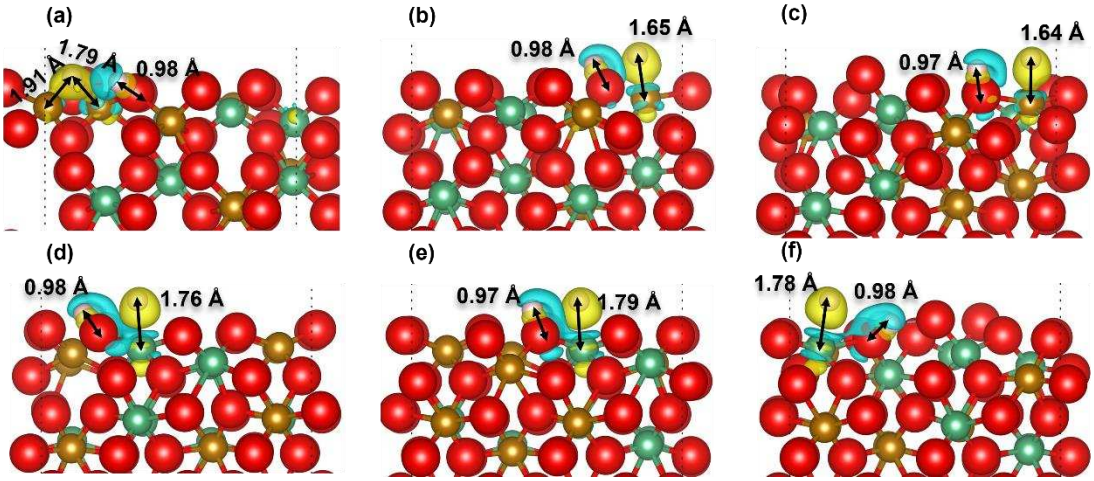

Figure 9. Charge transfer difference showing iso-surface level of 0.05 eV/Å^3 at the (a-c) Fe-O and (d-f) Nb-O sites of the (010) surfaces after dissociation of H_2; (a,d) Fe_3Nb_1-termination; (b,e) Fe_2Nb_2-termination; (c,f) Fe_1Nb_3-termination; (d) Fe_8Nb_8-termination; O atoms are red; Fe atoms are yellow; Nb atoms are green; H atoms are white; yellow color represents charge depletion and blue color represents charge gain.

Table 2. Bader charge (q) of the adsorbed H ions coordinated by Fe/Nb and O on the (010) surfaces.

	q_H (e)			
	Fe-O site		**Nb-O site (e)**	
	Fe-H	**O-H**	**Nb-H**	**O-H**
Fe_3Nb_1-termination	-0.21	+0.61	-0.32	+0.68
Fe_2Nb_2-termination	-0.29	+0.64	-0.37	+0.67
Fe_1Nb_3-termination	-0.19	+0.60	-0.37	+0.68

3.2.2 (111) surface

On the (111) surface, we found that five-fold cations are exposed in the top layers and we have therefore taken into account the seven adsorption sites, including two metal-oxygen sites that are similar to the (010) surfaces, and five oxygen-oxygen sites. For the oxygen-oxygen sites on the (111) surface, $O_{Fe/Nb}$ denotes the site where the two oxygen are coordinated by one five-fold cation, whereas in another type of reaction site, i.e. O_{Fe-Fe}, O_{Fe-Nb} and O_{Nb-Nb}, the two oxygen atoms are shared by two Fe/NbO_5 square pyramids, see Figure 10.

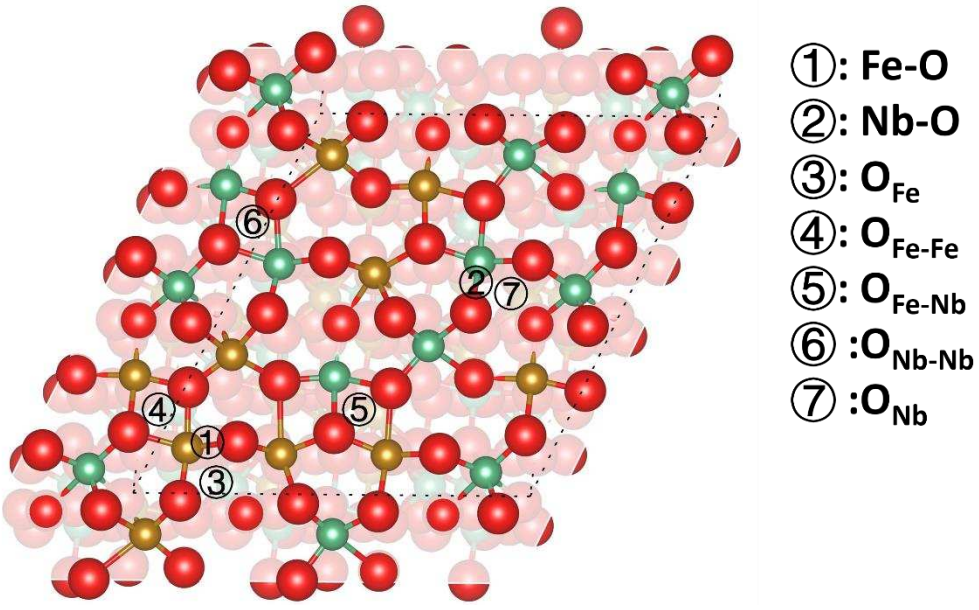

Figure 10. Dissociation sites of H_2 on the (111) surface; O atoms are red; Fe atoms are yellow; Nb atoms are green.

Figure 11 shows the dissociation reaction energy at the (111) surface under different

temperatures. We found that reactions at the O_{Fe} site are thermodynamically much more favourable than at the other three sites, with the dissociation energies remaining negative from 0 to 900 K, and they are even larger than those found for W-doped Al_2O_3 and WO_x materials[44,45]. At another oxygen site, *i.e.* the O_{Nb} site, the dissociation reaction is exothermic by -1.74 eV at 0 K but increases to ~0 eV when the temperature reaches 900 K. At the other sites, the reactions gradually become endothermic as the temperature increases, with the exception of the O_{Fe-Nb} site, where the dissociation energy is positive from 0 K upwards.

In general, our simulations indicate that the O_{Fe} site is the thermodynamically most favorable site on the (111) surface, and the priority of the reaction is the sequence: $E_{O_{Fe-Fe}} < E_{Nb-O} < E_{O_{Nb-Nb}} < E_{O_{Fe-Fe}} < E_{Fe-O} < E_{O_{Nb}} < E_{O_{Fe}}$. In addition, we found that the oxygen sites on the (111) surface have similar chemical activity to those on the (010) surfaces, but the Fe/Nb-O sites on the (111) surface are more active than on the (010) surfaces, suggesting that the five-fold cations exposed in the top layer play a more important role in the dissociation of H_2 than the four-fold cations.

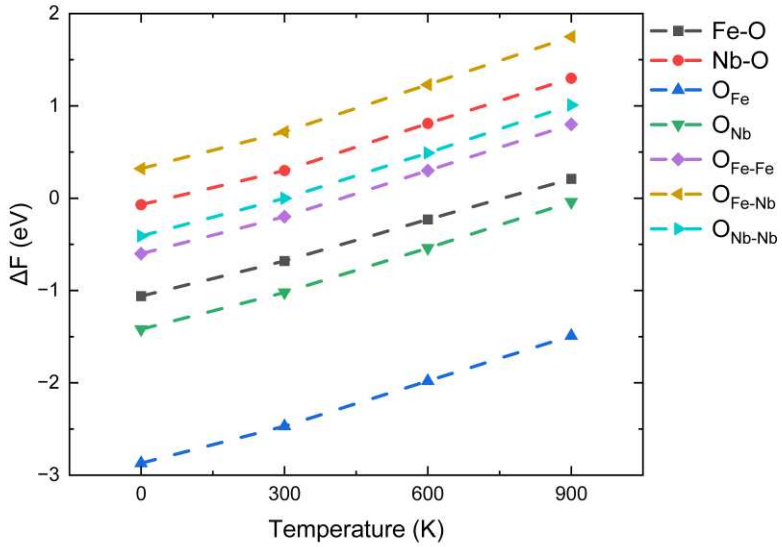

Figure 11. Dissociation energy of H_2 on the F_8N_8-terminated surface from 0 to 900 K.

The charge transfer at the Fe/Nb-O sites in the form of charge density difference plots are shown in Figure 12. Our simulations suggest partial electronic density transfer from

the cations to hydrogen at the Fe/Nb-O site and from hydrogen to oxygen at the O-H site, similar to the change of electronic distribution in the (010) surfaces. In addition, we found that the electron gain area around the Nb site is larger than that around the Fe site, in agreement with the larger Bader charge of -0.39 e for the H coordinated by Nb, see Table 3. The O-H bond lengths in the hydroxyl groups are close to 0.98 Å, whereas the Fe-H and Nb-H bonds at the Fe/Nb-O site are longer than the O-H by 0.58 and 0.82 Å, respectively. Compared with the (010) surfaces, we found that the differences in charge transfer, Bader charge and the bond length of the metal/oxygen-H between the (010) and (111) surfaces are small, with the exception of the Fe-O site of the (111) surface where the H coordinated by Fe has the smallest Bader charge of -0.16 e and the Fe-H has the shortest bond length at 1.56 Å.

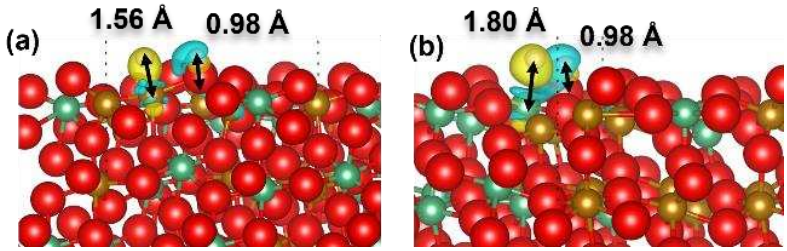

Figure 12. Charge transfer difference showing iso-surface level of 0.05 eV/Å^3 at the (a) Fe-O and (b) Nb-O sites of the (111) surface after dissociation of H_2; O atoms are red; Fe atoms are yellow; Nb atoms are green; H atoms are white; yellow color represents charge depletion and blue color represents charge gain.

Table 3. Bader charge (q) of the adsorbed H ions coordinated by Fe/Nb and O on the (111) surface.

	q_H (e)			
	Fe-O site (e)		**Nb-O site (e)**	
	Fe-H	**O-H**	**Nb-H**	**O-H**
Fe_8Nb_8-termination	-0.16	+0.62	-0.39	+0.63

3.3 Formation of Water

The dissociation of hydrogen at the surfaces revealed above shows that the formation of water could take place at both the Fe/Nb-O and O-O sites. To gain insight into the mechanism, we have chosen the Fe-O sites of the (010) surfaces and the O_{Fe} site of

411 the (111) surface to simulate the migration pathways of dissociated H atoms and the
412 water formation reactions. After dissociation on the (010) surfaces, the H atoms
413 coordinated to the Fe cations migrate towards the nearby oxygen ions to form a H_2O
414 molecule, which then desorbs from the surfaces, forming an oxygen vacancy in the top
415 layer, which in the SOFC process will be filled again by the oxygen ions from the
416 electrolyte. The proposed reaction process is shown in Figure 13.
417

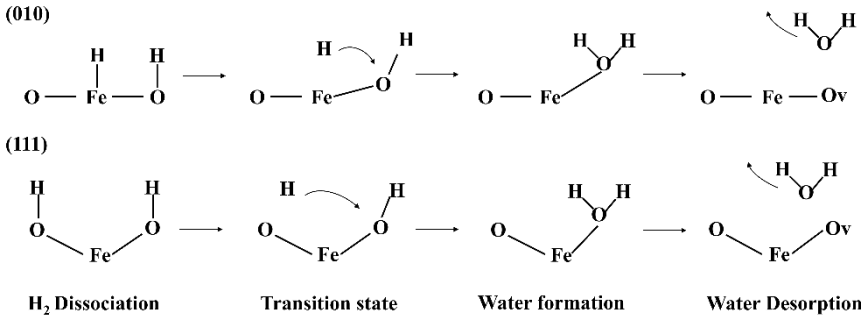

418
419 **Figure 13. Pathways of the water formation reaction on the (010) surface (top) and the (111)**
420 **surface (bottom); O and Fe indicate the atoms in the top surface layers, whereas Ov refers to an**
421 **oxygen vacancy.**

422

423 Figure 14 shows the hydrogen migration at the surfaces after dissociation on the top
424 layers. Our simulations show that the H_2O molecule is not stable on the Fe_3Nb_1
425 termination. Instead, one H atom tends to be captured by the adjacent oxygen ion,
426 forming a hydrogen-bond, leading to the two top O ions forming the hydroxyl groups
427 getting close to each other within a distance of 2.7 Å. In contrast, we found that the
428 H_2O molecules are stable on both the Fe_2Nb_2 and Fe_1Nb_3 terminations, where the bond
429 length of the nearby metal-oxygen on the Fe_1Nb_3 termination is longer by 0.3 Å
430 compared to the Fe_2Nb_2 termination. In addition, we found that the longest bond
431 distance of 3.12 Å is the (H)O(H)--Fe bond on the Fe_8Nb_8 (111) surface.
432 Overall, our calculations suggest that the surface-bound H_2O molecules, formed after
433 dissociation of the H_2 molecules, are generally stable at the surfaces, with the exception
434 of the Fe_3Nb_1 termination. These water molecules could leave the surfaces, as evidenced
435 by the lengthening of the metal-oxygen bonds compared to those in the bulk structure.[42]
436 We would suggest that the H atoms on the Fe_3Nb_1 termination (Fe-rich) preferring to

form two hydroxyl groups could be partially due to the oxygen ions in the Fe-rich region having a similar chemical activity towards the dissociated H atoms.

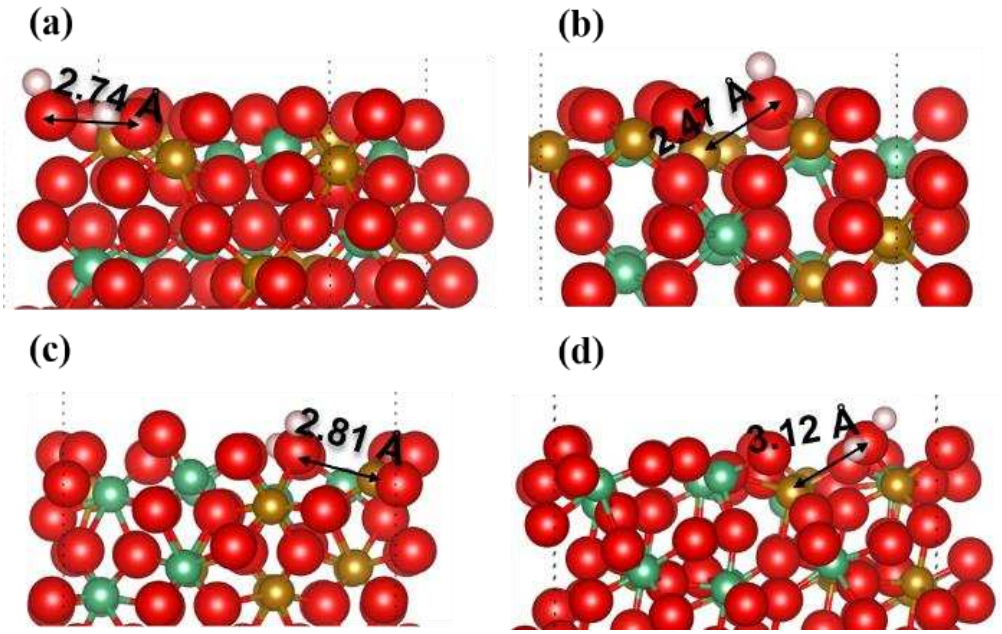

Figure 14. Optimized structures after the diffusion of H atoms on the four surfaces; (a) Fe-O site of the Fe_3Nb_1 terminated (010) surface; (b) Fe-O site of the Fe_2Nb_2 terminated surface; (c) Fe-O site of the Fe_1Nb_3 terminated surface ;(d) O_{Fe} site of the Fe_8Nb_8 terminated (111) surface; O atoms are red; Fe atoms are yellow; Nb atoms are green; H atoms are white.

The energy pathways are plotted in Figure 15. Our calculations show that the energy barriers from the dissociated *2H to the adsorbed H_2O* states (* indicates a surface-bound species) are in the range of 0.44 to 0.54 eV on the three (010) surfaces, compared to 1.08 eV on the Fe_8Nb_8-terminated (111) surface, which is still much lower than the migration barrier of 3.53 eV reported for the pure CeO_2 system[46]. In addition, the formation of the surface-bound water molecules is an energetically favourable process on the (010) surfaces, although on the (111) surface, the energy of the H_2O* state is similar to that of the *2H state. Finally, the desorption from the surfaces into a gaseous water molecule is also calculated, which is represented by the process from the H_2O* to the H_2O(g) state. The lowest barrier (1.02 eV) is found on the (111) surface, which is larger than the barrier found at the Ni-YSZ anode (~0.6 eV), but close to that found for the CeO_2 material (~0.9 eV)[46-48], indicating that the $FeNbO_4$ phase exhibits catalytic properties that are compatible to those two commonly used SOFC anode materials,

where the dissociation of hydrogen is concerned.

Overall, our simulations indicate that migration of the dissociated H atoms on the (111) surface needs to overcome a larger barrier than on the (010) surfaces to form the surface-bound water molecules, which can be explained by the fact that the O-H bond is stronger than the Fe-O, in agreement with the analysis of the Bader charges. In addition, we found that water formation on the Fe_3Nb_1 termination is more endothermic than on other surfaces, indicating that forming gaseous water molecules through two hydroxyl groups is energetically difficult compared to the directly bonded water molecules.

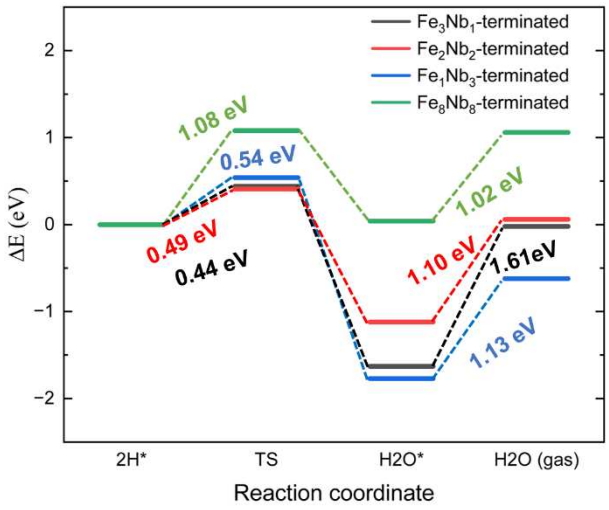

Figure 15. Energy pathways of diffusion of H and water formation on the four surfaces; TS refers to the transition state from H_2 dissociation to H_2O formation; * refers to the surface-bound state, and the energies shown for the two steps refer to the energy barriers from 2H* to TS and H2O* to H2O (gas), respectively.

4. Conclusions

We have employed DFT+U-D2 calculations to investigate the surface properties of the orthorhombic $FeNbO_4$ material, the adsorption and dissociation of H_2 molecules, the migration of H ions, as well as the formation of water at the (010) and (111) surfaces. First, the calculations of the surface properties have demonstrated that the five-fold cations in the (111) surface show a higher oxidation state than the four-fold cations in the (010) surfaces, and the bandgaps of those surfaces are reduced to less than 0.5 eV.

The interplanar relaxations indicate that the first two top layers of the three (010) surfaces move in opposite directions, leading to the metal cations in the sub-surface layers becoming exposed to the vacuum, whereas the relaxed two layers of the (111) surface shift outwards from the bulk. We have selected the Fe/Nb-O and O-O sites on the (010) and (111) surfaces as the dissociation sites for the H_2 molecule. At the Fe/Nb-O sites, the five-fold cations of the (111) surface enable dissociation more readily than the four-fold Fe/Nb in the (010) surfaces. In addition, our calculations indicate that the numbers of Fe cations coordinated to the O can affect the dissociation energies. Specifically, dissociation at the $O_{FeFe-FeFe}$ and $O_{FeFe-FeNb}$ sites of the (010) surfaces remains exothermic from 0 to 900 k, whereas the reaction at other sites becomes endothermic at temperatures below 900 K. Similarly, we found that the hydrogen molecule prefers to dissociate at the O_{Fe} site of the (111) surface, where the reactions remain exothermic in the range of 0 to 900 K. Charge transfer investigations at the Fe/Nb-O sites have shown that on both the (010) and (111) surfaces the H atoms obtain electron density from Fe/Nb, whereas the electrons are transferred from the other dissociated H atom to the coordinated O atom.

Finally, we have simulated the migration of H ions and the formation of water at the Fe-O sites in the (010) surface and the O_{Fe} site of the (111) surface. The barriers for the diffusion of H ions range from 0.44 to 0.54 eV on the three (010) surfaces, but is higher at 1.08 eV on the (111) surface. The lowest calculated barrier for the formation of surface-bound water is found for the O_{Fe} site of the (111) surface at 1.02 eV, which is close to that of other anode materials, e.g. Ni-YSZ and CeO_2.

Overall, our simulations suggest that the oxygen bridge sites both on the (010) and (111) surfaces display more chemical reactivity towards H_2 dissociation than the metal-oxygen bridge sites. However, the diffusion of dissociated H ions from the oxygen bridge sites is energetically less favorable than from the Fe/Nb-O sites.

We consider that this work, which has revealed the mechanisms of hydrogen dissociation and water formation at individual sites on two major surfaces of disordered o-$FeNbO_4$, shows that this material has promising characteristics for SOFC anode

applications. For example, our findings have revealed that $FeNbO_4$ offers several thermodynamic and kinetic advantages: (i) the relatively low energy barriers for hydrogen dissociation and water formation on key surfaces, (ii) the stability of the surface-bound H atoms in the form of hydroxyl groups, and (iii) the low bandgap values at the surfaces, which indicate enhanced electronic conductivity. In addition, the five-fold coordination of Fe and Nb on the (111) surface significantly improves the dissociation of H_2, indicating strong reactivity at these sites. We consider that these features position $FeNbO_4$ as a potential alternative to Ni-based anodes. We trust that our study will provide guidance for future experimental work.

5. Acknowledgements

XW acknowledges the China Scholarship Council (CSC) for award No. 201906460008 and the University of Leeds for a PhD scholarship. This work has used the computing resources from the Supercomputing Wales project, which is partly funded by the European Regional Development Fund (ERDF), and the high performance computing facilities (ARC4) provided by the University of Leeds. We also acknowledge computing resources on the UK's national supercomputing service ARCHER2 facility (http://www.archer2.ac.uk) via our membership of the UK's HEC Materials Chemistry Consortium, which is funded by EPSRC (EP/L000202).

References

1. Dwivedi, S., Solid Oxide Fuel Cell: Materials for Anode, Cathode and Electrolyte. *International Journal of Hydrogen Energy* **2020**, *45*, 23988-24013.
2. Ramadhani, F.; Hussain, M. A.; Mokhlis, H.; Hajimolana, S., Optimization Strategies for Solid Oxide Fuel Cell (SOFC) Application: A Literature Survey. *Renewable and Sustainable Energy Reviews* **2017**, *76*, 460-484.
3. Hussain, S.; Yangping, L., Review of Solid Oxide Fuel Cell Materials: Cathode, Anode, and Electrolyte. *Energy Transitions* **2020**, *4*, 113-126.
4. Shaikh, S. P. S.; Muchtar, A.; Somalu, M. R., A Review on the Selection of Anode Materials for Solid-Oxide Fuel Cells. *Renewable and Sustainable Energy Reviews* **2015**, *51*, 1-8.
5. Zhu, W. Z.; Deevi, S. C., A Review on the Status of Anode Materials for Solid Oxide Fuel Cells. *Materials Science and Engineering: A* **2003**, *362*, 228-239.
6. Shu, L.; Sunarso, J.; Hashim, S. S.; Mao, J.; Zhou, W.; Liang, F., Advanced Perovskite Anodes for Solid Oxide Fuel Cells: A Review. *International Journal of Hydrogen Energy* **2019**, *44*, 31275-31304.
7. An, W.; Men, Y.; Wang, J., Comparative Study on Hydrogenation of Propanal on Ni(111) and Cu(111) from Density Functional Theory. *Applied Surface Science* **2017**, *394*, 333-339.
8. Zhu, H.; Hou, Y.; Ren, H.; Liu, D.; Li, X.; Zhao, L.; Chi, Y.; Guo, W., Theoretical Investigation on H2 Oxidation Mechanisms over Pristine and Sm-Doped CeO_2(1 1 1) Surfaces. *Applied Surface Science* **2020**, *511*.
9. Liu, Z.; Wang, B.; Cazorla, C., Mechanical and Electronic Properties of CeO_2 under Uniaxial Tensile Loading: A Dft Study. *Materialia* **2021**, *15*.
10. Li, S.; Lu, Z.; Yang, Z.; Chu, X.; Zhang, Y.; Ma, D., The Sulfur Tolerance Mechanism of the Cu/ CeO_2 System. *International Journal of Hydrogen Energy* **2014**, *39*, 1957-1966.
11. García-Melchor, M.; López, N., Homolytic Products from Heterolytic Paths in H2 Dissociation on Metal Oxides: The Example of CeO_2. *The Journal of Physical Chemistry C* **2014**, *118*, 10921-10926.
12. M., S.; T., Z., The Electronic Structure and Chemical Properties of a Ni/ CeO_2 Anode in a Solid Oxide Fuel Cell: A Dft + U Study. *The Journal of Physical Chemistry C* **2010**, *114*, 21411–21416.
13. Chung, Y. S.; Kim, T.; Shin, T. H.; Yoon, H.; Park, S.; Sammes, N. M.; Kim, W. B.; Chung, J. S., In Situ Preparation of a La1.2sr0.8mn0.4fe0.6o4 Ruddlesden–Popper Phase with Exsolved Fe Nanoparticles as an Anode for Sofcs. *Journal of Materials Chemistry A* **2017**, *5*, 6437-6446.
14. Kousi, K.; Tang, C.; Metcalfe, I. S.; Neagu, D., Emergence and Future of Exsolved Materials. *Small* **2021**, *17*, e2006479.
15. Teng, Z.; Xiao, Z.; Yang, G.; Guo, L.; Yang, X.; Ran, R.; Wang, W.; Zhou, W.; Shao, Z., Efficient Water Splitting through Solid Oxide Electrolysis Cells with a New Hydrogen Electrode Derived from a-Site Cation-Deficient $La_{0.4}Sr_{0.55}Co_{0.2}Fe_{0.6}Nb_{0.2}O_{3-\Delta}$ Perovskite. *Materials Today Energy* **2020**, *17*.
16. Cowin, P. I.; Lan, R.; Zhang, L.; Petit, C. T. G.; Kraft, A.; Tao, S., Study on Conductivity and Redox Stability of Iron Orthovanadate. *Materials Chemistry and Physics* **2011**, *126*, 614-618.
17. Ni, C.; Feng, J.; Cui, J.; Zhou, J.; Ni, J., Ann-Type Oxide $Fe_{0.5}Mg_{0.25}Ti_{0.25}Nb_{0.9}Mo_{0.1}O_{4-\Delta}$ for Both

Cathode and Anode of a Solid Oxide Fuel Cell. *Journal of The Electrochemical Society* **2017**, *164*, F283-F288.

18. Liu, X.; Zhou, J.; Xie, D.; Ni, J.; Ni, C., Fenbo4-Based Oxide Cathode for Steam Electrolysis. *Solid State Ionics* **2020**, *345*.

19. Liu, X.; Xie, D.; Irvine, J. T. S.; Ni, J.; Ni, C., An $FeNbO_4$-Based Oxide Anode for a Solid Oxide Fuel Cell (SOFC). *Electrochimica Acta* **2020**, *335*.

20. Wang, X.; Santos-Carballal, D.; de Leeuw, N. H., Density Functional Theory Study of Monoclinic $FeNbO_4$: Bulk Properties and Water Dissociation at the (010), (011), (110), and (111) Surfaces. *The Journal of Physical Chemistry C* **2021**, *125*, 27566-27577.

21. Marrocchelli, D.; Yildiz, B., First-Principles Assessment of H_2S and H_2O Reaction Mechanisms and the Subsequent Hydrogen Absorption on the Ceo2(111) Surface. *The Journal of Physical Chemistry C* **2012**, *116*, 2411-2424.

22. Kresse, G.; Furthmiiller, J., Efficiency of Ab-Initio Total Energy Calculations for Metals and Semiconductors Using a Plane-Wave Basis Set. *Computational Materials Science* **1996**, *6*, 15-20.

23. Kresse, G.; Furthmuller, J., Efficient Iterative Schemes for Ab Initio Total-Energy Calculations Using a Plane-Wave Basis Set. *Physical Review B - Condensed Matter* **1996**, *54*, 11169-11186.

24. Kresse, G.; Hafner, J., Ab Initio Molecular Dynamics for Open-Shell Transition Metals. *Physical Review B - Condensed Matter* **1993**, *48*, 13115-13118.

25. Kresse, G.; Hafner, J., Norm-Conserving and Ultrasoft Pseudopotentials for First-Row and Transition Elements. *Journal of Physics: Condensed Matter* **1994**, *6*, 8245-8260.

26. Blochl, P. E., Projector Augmented-Wave Method. *Physical Review B - Condensed Matter* **1994**, *50*, 17953-17979.

27. Perdew, J. P.; Burke, K.; Ernzerhof, M., Generalized Gradient Approximation Made Simple. *Physical Review Letters* **1996**, *77*, 3865-3868.

28. Dudarev, S. L.; Botton, G. A.; Savrasov, S. Y.; Humphreys, C. J.; Sutton, A. P., Electron-Energy-Loss Spectra and the Structural Stability of Nickel Oxide: An Lsda+u Study. *Physical Review B* **1998**, *57*, 1505-1509.

29. Liao, P.; Carter, E. A., Testing Variations of the Gw Approximation on Strongly Correlated Transition Metal Oxides: Hematite (Alpha-Fe_2O_3) as a Benchmark. *Phys Chem Chem Phys* **2011**, *13*, 15189-99.

30. Lee, J.; Han, S., Thermodynamics of Native Point Defects in Alpha-Fe_2O_3: An Ab Initio Study. *Phys Chem Chem Phys* **2013**, *15*, 18906-14.

31. Henkelman, G.; Arnaldsson, A.; Jónsson, H., A Fast and Robust Algorithm for Bader Decomposition of Charge Density. *Computational Materials Science* **2006**, *36*, 354-360.

32. van de Walle, A., Multicomponent Multisublattice Alloys, Nonconfigurational Entropy and Other Additions to the Alloy Theoretic Automated Toolkit. *Calphad* **2009**, *33*, 266-278.

33. van de Walle, A.; Asta, M.; Ceder, G., The Alloy Theoretic Automated Toolkit: A User Guide. *Calphad: Comput. Coupling Phase Diagrams Thermochem.* **2002**, *26*, 539-553.

34. van de Walle, A.; Tiwary, P.; de Jong, M.; Olmsted, D. L.; Asta, M.; Dick, A.; Shin, D.; Wang, Y.; Chen, L. Q.; Liu, Z. K., Efficient Stochastic Generation of Special Quasirandom Structures. *Calphad* **2013**, *42*, 13-18.

35. Grau-Crespo, R.; Hamad, S.; Catlow, C. R. A.; de Leeuw, N. H., Symmetry-Adapted Configurational Modelling of Fractional Site Occupancy in Solids. *Journal of Physics: Condensed Matter* **2017**, *19*.

36. Watson, G. W.; Toby Kelsey, E.; de Leeuw, N. H.; Harris, D. J.; Parker, S. C., Atomistic Simulation of Dislocations, Surfaces and Interfaces in Mgo. *Journal of the Chemical Society, Faraday Transactions* **1993**, *92*, 433-438.
37. Grimme, S., Semiempirical Gga-Type Density Functional Constructed with a Long-Range Dispersion Correction. *J Comput Chem* **2006**, *27*, 1787-99.
38. Tersoff, J.; Hamann, D. R., Theory and Application for the Scanning Tunneling Microscope. *Phys. Rev. Lett.* **1983**, *50*, 1998-2001.
39. Wang, N. Xu, J.C. LIU, G. Tang, et al, VASPKIT: A Pre-and Post-Processing Program for VASP Code, arXiv:1908.08269.
40. C., L. D.; Jorge, N., On the Limited Memorybfgs Method for Large Scale Optimization. *Mathematical Programming* **1989**, *45*, 503-528.
41. M. W. J. Chase, NIST JANAF Termochemical Tables, American Chemical Society and American Institute of Physics for the National Institute of Standards and Technology, Washington DC, 1998
42. Ananta, S.; Brydson, R.; Thomas, N. W., Synthesis, Formation and Characterisation of Fenbo4 Powders. *Journal of the European Ceramic Society* **1999**, *19*, 489-496.
43. Dhak, P.; Dhak, D.; Das, M.; Subashchandrabose, T.; Pramanik, P., A Novel Synthesis of Fenbo4 Nanorod by Hydrothermal Process. *Journal of Nanoparticle Research* **2011**, *13*, 4153-4159.
44. Saritha, D., Sol-Gel Synthesis and Electrochemical Properties of Wolframite Fenbo4. *Journal of Physics: Conference Series* **2020**, *1495*.
45. Jimenez-Orozco, C.; Flórez, E.; Rodriguez, J. A., The A-Wc(0001) Surface as a Hydrogen Sponge: A First Principle Study of H2 Dissociation and Formation of Low and High Coverages. *ChemCatChem* **2023**, *15*.
46. Long, Q.; Guo, C.; Xin, X.; Ding, R.; Luo, L.; Zhang, X.; Li, H.; Cui, Z.; Xu, Y.; Tang, C., Spontaneous Dissociation of H_2 and High Energy Barrier of H Invasion on W Doped Al_2O_3(0001) Surface. *International Journal of Hydrogen Energy* **2022**, *47*, 1076-1082.
47. Zhu, H.; Hou, Y.; Ren, H.; Liu, D.; Li, X.; Zhao, L.; Chi, Y.; Guo, W., Theoretical Investigation on H2 Oxidation Mechanisms over Pristine and Sm-Doped CeO_2(1 1 1) Surfaces. *Applied Surface Science* **2020**, *511*.
48. García-Melchor, M.; López, N., Homolytic Products from Heterolytic Paths in H_2 Dissociation on Metal Oxides: The Example of CeO_2. *The Journal of Physical Chemistry C* **2014**, *118*, 10921-10926.
49. Deleebeeck, L.; Shishkin, M.; Addo, P.; Paulson, S.; Molero, H.; Ziegler, T.; Birss, V., Activation of H(2) Oxidation at Sulphur-Exposed Ni Surfaces under Low Temperature Sofc Conditions. *Phys Chem Chem Phys* **2014**, *16*, 9383-93.